arXiv:1408.2183v1 [cond-mat.mtrl-sci] 10 Aug 2014

Large linear magnetoresistance in the Dirac semimetal TlBiSSe

Mario Novak,* Satoshi Sasaki, Kouji Segawa, and Yoichi Ando†
Institute of Scientific and Industrial Research, Osaka University, Ibaraki, Osaka 567-0047, Japan
(Dated: August 12, 2014)

The mixed-chalcogenide compound TlBiSSe realizes a three-dimensional (3D) Dirac semimetal state. In clean, low-carrier-density single crystals of this material, we found Shubnikov-de Haas oscillations to signify its 3D Dirac nature. Moreover, we observed very large linear magnetoresistance (MR) approaching 10,000% in 14 T at 1.8 K, which diminishes rapidly above 30 K. Our analysis of the magnetotransport data points to the possibility that the linear MR is fundamentally governed by the Hall field; although such a situation has been predicted for highly-inhomogeneous systems, inhomogeneity does not seem to play an important role in TlBiSSe. Hence, the mechanism of large linear MR is an intriguing open question in a clean 3D Dirac system.

PACS numbers: 72.20.My, 75.47.De, 71.20.Nr, 72.80.Jc

The discoveries of graphene [1] and three-dimensional (3D) topological insulators [2–4] greatly advanced the physics of two-dimensional (2D) massless Dirac fermions. In comparison, 3D massless Dirac fermions, whose Hamiltonian involves all three Pauli matrices, have attracted much less attention. This is due partly to the shortage of concrete materials to give access to the massless Dirac physics in 3D, although *massive* 3D Dirac fermions in Bi are long known to present interesting physics [5–7]. However, this situation has changed recently, and materials to realize 3D massless Dirac fermions are currently attracting significant attention because of the interest in a new type of topological materials called Weyl semimetals [8, 9]. In recent literature, materials realizing spin-degenerate 3D massless Dirac fermions are called "3D Dirac semimetal", while those realizing a pair of spin-nondegenerate 3D massless fermions are called "Weyl semimetal"; the latter is derived from the former by breaking time-reversal symmetry or space-inversion symmetry (or both) to split the spin-degenerate Dirac cone into two spin-nondegenerate ones [9].

Recently, the 3D Dirac semimetal phase has been shown to exist in Na_3Bi [10–12] and Cd_3As_2 [13–15]. Also, such a phase is known to exist at the topological phase transition point of $TlBi(S_{1-x}Se_x)_2$ [16–19], $Pb_{1-x}Sn_xSe$ [20], $Bi_{1-x}Sb_x$ [21] etc., where the bulk band gap necessarily closes. In those materials, the Weyl semimetal phase would be realized by magnetic doping, breaking the crystal inversion symmetry, or applying external magnetic field [18, 19, 22, 23]. Besides being potential parent materials of Weyl semimetals, the Dirac semimetals offer a new playground to explore the physics of massless Dirac fermions in larger spatial degrees of freedom than the 2D case, which may change the characteristic transport properties in a nontrivial way.

In this Letter, we report our magnetotransport studies of TlBiSSe, where the 3D Dirac semimetal phase is realized as a result of the topological phase transition between the topological insulator (TI) $TlBiSe_2$ and an ordinary insulator $TlBiS_2$ [16, 17]. In TlBiSSe, as the Fermi level is tuned close to the Dirac point, the magnetoresistance (MR) grows very rapidly, and its magnetic-field dependence is found to become linear in high magnetic fields. Surprisingly, in samples with the Fermi energy E_F of about 20 meV, we observed very large linear MR approaching 10,000% at 14 T. Our analysis of the magnetotransport data strongly suggests that the linear MR is somehow governed by the Hall field, but its origin is not explicable with existing theories for linear MR, pointing to new physics peculiar to 3D Dirac fermions.

The TI nature of $TlBiSe_2$ was found in 2010 [24–26], and the existence of the topological phase transition in $TlBi(S_{1-x}Se_x)_2$ was discovered in 2011 [16, 17]: according to the angle-resolved photoemission spectroscopy (ARPES) data, the bulk band gap in $TlBi(S_{1-x}Se_x)_2$ closes at $x = 0.5$, across which the band inversion takes place and the $x > 0.5$ side obtains nontrivial Z_2 topology signified by the appearance of topological surface states. This means that the zero-gap semimetallic state is realized in TlBiSSe, in which S and Se occupy the chalcogen site in a mixed way. Single crystals of $TlBi(S_{1-x}Se_x)_2$ grown from stoichiometric melts are always n-type with the typical carrier density of 10^{20} cm^{-3} [24]. Motivated by a recent report [27], we have grown crystals of TlBiSSe with a Tl-rich starting composition [28], and succeeded in reducing the bulk carrier density down to 10^{17} cm^{-3} level. High crystallinity of our single crystals is confirmed by x-ray diffraction (XRD) analysis [Fig. 1(a)] and Laue analysis. Although the crystals are grown from off-stoichiometric melts, inductively-coupled plasma atomic-emission spectroscopy (ICP-AES) analysis confirmed that the compositions of the grown crystals are close to stoichiometry, and electron-probe microanalysis (EPMA) data assured that there is no segregation of constituent elements, as discussed in the Supplemental Material [28]. Experimental details of our transport measurements are also described in [28].

The temperature dependencies of the in-plane resistivity, $\rho_{xx}(T)$, of three representative TlBiSSe samples with significantly different carrier densities are shown in

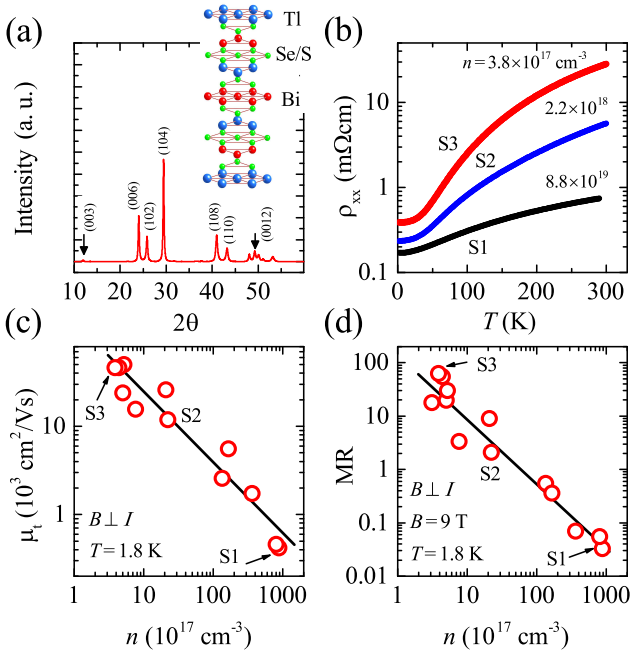

FIG. 1: (a) Powder XRD pattern of a typical TlBiSSe crystal; inset shows its crystal structure. (b) $\rho_{xx}(T)$ behavior of three samples with different carrier densities. (c, d) Plots of low-temperature mobility and the magnitude of MR vs n. The MR values shown here are for 9 T at 1.8 K.

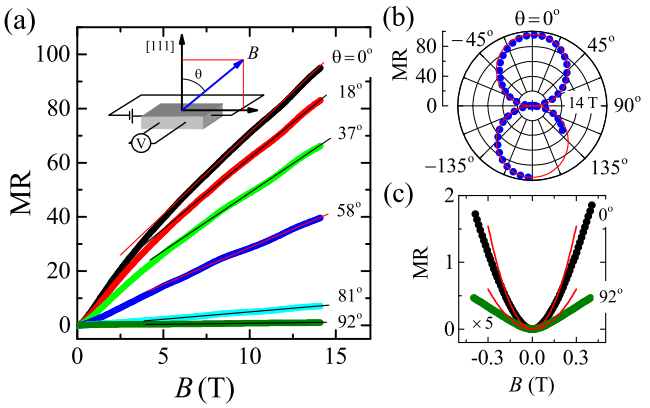

FIG. 2: MR in sample S3 at 1.8 K. (a) $\rho_{xx}(B)$ behavior for various magnetic-field angles form transverse ($\theta = 0°$, B field in the [111] direction) to the near-longitudinal ($\theta = 92°$) configurations; inset depicts the definition of θ. (b) Dipole-like θ dependence of the magnitude of MR at 14 T, which follows the $\cos\theta$ dependence (red solid line). Due to the restriction of the rotation stage, the range of θ does not span the whole 360°. (c) Low-field MR showing ordinary B^2 behavior; the red solid lines show the fits to the B^2 function.

Fig. 1(b); note that the vertical axis is in logarithmic scale, and the residual resistivity ratio of the lowest-carrier-density sample (S3) is as large as 73. We have actually measured many more samples than are shown in Fig. 1(b), and Fig. 1(c) shows that the low-temperature transport mobility μ_t (assessed from ρ_{xx} at 1.8 K and the carrier density n) increases systematically with decreasing n; for example, μ_t increases by 110 times between samples S1 ($n = 8.8 \times 10^{19}$ cm^{-3}) and S3 ($n = 3.8 \times 10^{17}$ cm^{-3}). This is in contrast to the case of 2D Dirac systems like graphene [29] and 3D TIs [30], where μ_t shows an enhancement only when the Fermi level is tuned very close to the Dirac point.

Perhaps more surprising is the very rapid increase in MR with decreasing n; for example, the MR at 9 T [Fig. 1(d)] changes by almost 2,000 times between S1 and S3. Here, MR is defined by $[\rho_{xx}(B) - \rho_{xx}(0\,\mathrm{T})]/\rho_{xx}(0\,\mathrm{T})$. To gain insights into the large MR, Fig. 2(a) shows how the MR behavior in sample S3 changes when the magnetic field is tilted from perpendicular to parallel directions. The angular dependence is more directly shown in Fig. 2(b), where the magnitude of the MR in 14 T is plotted as a function of the angle θ, which is defined in the inset of Fig. 2(a). The dipole-like pattern seen in Fig. 2(b) is well described by the $\cos\theta$ function (red solid line), meaning that the MR is almost entirely governed by the perpendicular component of the magnetic field, even though the present system is 3D. The magnetic-field dependence of ρ_{xx} at low field is plotted in Fig. 2(c) for $\theta = 0°$ and 92°, both of which present the ordinary B^2 behavior below ~0.1 T; this suggests that the origin of the linear MR is different from the famous linear MR in $Ag_{2+\delta}Se$ and $Ag_{2+\delta}Te$ [31], where the linearity is observed from as low as 1 mT. Note that, due to the high mobility of the sample S3, the condition $\omega_c\tau_t = \mu_t B = 1$ (τ_t is the transport scattering time and $\omega_c = eB/m_c$ is the cyclotron frequency with m_c the cyclotron mass) is achieved in only 0.2 T, and hence the standard theory for MR for a closed Fermi surface [32] would predict a saturation at $B \gg 0.2$ T; nevertheless, as one can see in Fig. 2(a), this sample presents non-saturating linear MR above ~6 T.

The temperature dependence of this linear MR signifies its unique nature, not reported before for other systems showing large linear MR [31, 33–37]. Figures 3(a)-3(c) show ρ_{xx} vs B at various temperatures, where one can see that the characteristic field above which the linear MR is observed remains around 6 T up to 150 K, but at higher temperature the linear MR disappears. More importantly, the size of MR changes little between 1.8 and 30 K, but at higher temperature it diminishes rapidly. This temperature dependence is summarized in Fig. 3(d), where the dependence of n on temperature is plotted together; one can see that n changes only by a small amount, and hence the rapid decline in MR has little to do with the thermal activation of carriers. On the other hand, as shown in Fig. 3(e), the size of MR depends linearly on μ_t, implying that the reason for the rapid decline in MR is the phonon scattering which restricts μ_t at high temperature.

It is prudent to mention that, even though the MR is unusual in many respect, it obeys the Kohler's rule [32]

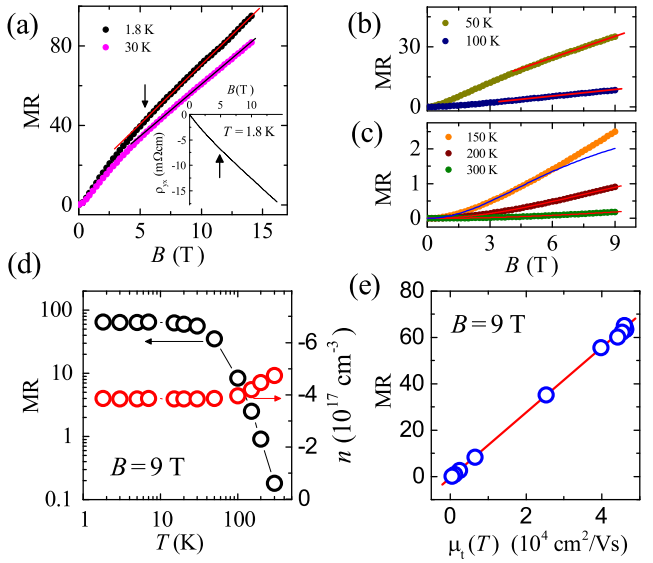

FIG. 3: MR in sample S3 for $\theta = 0°$. (a, b, c) $\rho_{xx}(B)$ behavior at various temperatures; note the different vertical scales between panels. The inset in (a) shows the $\rho_{yx}(B)$ behavior at 1.8 K; the arrows mark the change in slope. The straight lines in (a) and (b) are fits to the linear part, while the solid lines in (c) are fits of the low-field part to the classical $aB^2/(1+bB^2)$ law. (d) Temperature dependences of the magnitude of MR at 9 T (left axis) and the carrier density calculated from R_H at each T (right axis). (e) Plot of the magnitude of MR at 9 T vs the transport mobility μ_t, which changes with T.

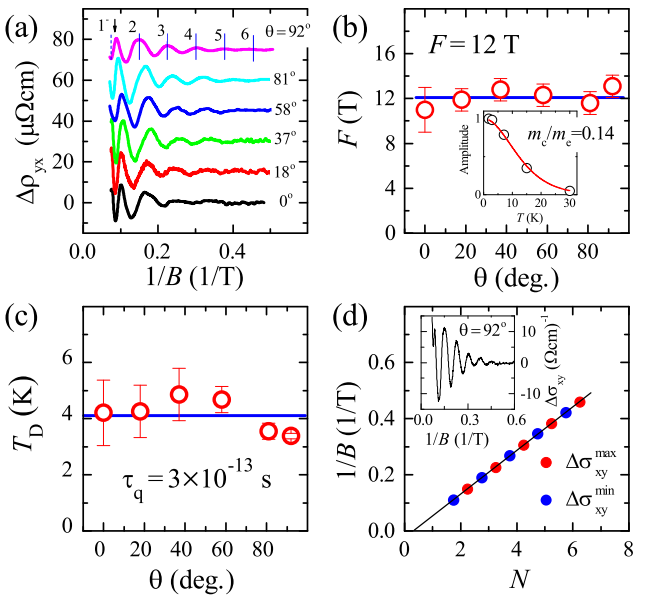

FIG. 4: SdH oscillations in sample S3. (a) SdH oscillations in ρ_{yx} vs $1/B$ at 1.8 K for various magnetic-field directions. The equidistant maxima are indicated by vertical lines, with the exception of the 1st Landau level which shows spin splitting. (b) θ dependence of the oscillation frequency; inset shows the temperature dependence of the oscillation amplitude for $\theta = 0°$ together with the fitting to the Lifshitz-Kosevich theory which gives $m_c/m_e = 0.14$. (c) θ dependence of the Dingle temperature. (d) Landau-level index plot for oscillations in σ_{xy} measured at 1.8 K and $\theta = 0°$; inset shows the oscillations in $\Delta\sigma_{xy}$ which is obtained by subtracting a smooth background from σ_{xy}. Following the principle in Refs. [4, 44] and assuming electron carriers, we assign the index $N + \frac{1}{4}$ and $N + \frac{3}{4}$ to the maxima and minima in $\Delta\sigma_{xy}$, respectively. Solid line is a linear fitting to the data, giving the intercept on the N axis of 0.34.

(see [28] for details), meaning that ρ_{xx} depends on the magnetic field only through the form $B\tau_t$ (which is the case in the semiclassical relaxation-time approximation). In passing, the MR data at 200 and 300 K can be described by the conventional form $aB^2/(1+bB^2)$ [38].

The low-carrier-density samples are clean enough to present Shubnikov-de Haas (SdH) oscillations, which are the source of the wiggles in the MR data at high B. Clear observation of SdH oscillations signifies not only a high mobility but also a high homogeneity of local carrier density, since a variation of local carrier density would result in a spread of SdH frequencies to smear the oscillations. In the case of TlBiSSe, a larger number of oscillation cycles are discernible in $\rho_{yx}(B)$ than in $\rho_{xx}(B)$, so we mainly used the former for the following analysis. Figure 4(a) shows SdH oscillations in ρ_{yx} for varying magnetic-field angle θ after removing the linear background. The Fourier transform gives only one frequency, whose dependence on θ is shown in Fig. 4(b); these data reveal a very small spherical (isotropic) Fermi surface (FS).

The averaged frequency $F = 12$ T gives the FS radius $k_F^{3D} = 1.9 \times 10^6$ cm^{-1} and the carrier density $n_{\rm SdH} = 2.4 \times 10^{17}$ cm^{-3} [39]. From the temperature dependence of the oscillation amplitude at $\theta = 0°$ [Fig. 4(b) inset], we obtain $m_c = 0.14m_e$ (m_e is the free electron mass) by using the Lifshitz-Kosevich (LK) theory [40]. This allows us to determine the Dingle temperature $T_{\rm D}$, which is plotted in Fig. 4(c) as a function of θ. Its average value, $T_{\rm D} = 4.1$ K, gives the quantum scattering time $\tau_q = \hbar/(2\pi k_B T_{\rm D}) = 3 \times 10^{-13}$ s. This is to be compared with the transport scattering time $\tau_t = 3.7 \times 10^{-12}$ s assessed from μ_t; the difference, which in this case is about 10 times, is usually associated with the difference in the rates between forward and backward scatterings [41]; obviously, small-angle (forward) scatterings are relatively strong in TlBiSSe, which happens when weak scattering potentials predominate. Other parameters of interest are obtained as follows: the quantum mobility $\mu_q \equiv e\tau_q/m_c \approx 3500$ cm^2/Vs, Fermi velocity $v_F = \hbar k_F/m_c = 1.6 \times 10^5$ m/s, and the Fermi energy (measured from the Dirac point) $E_F = \hbar v_F k_F = 20$ meV.

An important information derived from SdH oscillations is the Berry phase [4, 42, 43]. We made the Landau-level (LL) index plot based on the positions of minima and maxima in σ_{xy} [44] as a function of $1/B$ [Fig. 4(d) inset]. In a system with 3D FS, the intercept of the in-

dex plot on the N axis is expected to be $0 \pm 1/8$ for Schrödinger fermions, while it should be $1/2 \pm 1/8$ for Dirac fermions (the sign before $1/8$ should be + for holes and − for electrons) [42, 43]. In our case, the intercept is 0.34 [Fig. 4(d)], which is close to $1/2 - 1/8 = 0.375$ and hence is consistent with 3D Dirac electrons.

We now discuss the possible mechanism of the observed large linear MR. There are several theoretical models which predict linear MR for low-carrier-density systems. Abrikosov [45, 46] proposed a quantum interpretation of the phenomena by assuming a gapless linear dispersion and the system to be in the ultra-quantum limit. The main feature of this model, apart from the linear MR, is the stability against temperature; this is because the condensation to the lowest LL is robust until level broadening causes an overlap of adjacent LLs. TlBiSSe is a gapless 3D Dirac system, and thus the Abrikosov model of quantum linear MR would be appropriate for describing the observed linear MR. In this regard, the linear MR in the transverse orientation ($\theta = 0^\circ$) sets in at ∼6 T, which corresponds to the situation when the Fermi level is in the 2nd LL; such a situation was previously argued to be sufficiently close to the ultra-quantum limit to observe the quantum MR [33–35]. However, the strong decrease of the MR above ∼30 K [Fig. 3(d)] contradicts the Abrikosov's model.

Thus we turn to other models which can predict linear non-saturating MR in a system with small 3D FS. A classical one is by Herring [47], who developed a perturbation theory for a system with weak inhomogeneity in the carrier density and showed that the fluctuations in the Hall field due to the inhomogeneity will lead to linear MR. Parish and Littlewood (PL) [48, 49] proposed a more comprehensive model which is valid also in the strong inhomogeneity limit and showed that the inhomogeneity will cause distortions in the current paths, which in turn causes the Hall field to contribute to the MR in a symmetric manner with respect to $\pm B$. In this respect, the θ dependence of the MR [Fig. 2(b)], which suggests that only the perpendicular component of the magnetic field is responsible for the MR, seems to support the scenario that the linear MR originates from the Hall field. Moreover, the data for in-plane magnetic field rotation (described in the Supplemental Material [28]) are also consistent with this scenario. In addition, it is suggestive that a change in slope of $\rho_{xx}(B)$ that occurs at around 5 T seems to be correlated with a similar change in slope of $\rho_{yx}(B)$ at the same field [Fig. 3(a)].

An important clue comes from the Hall angle $\theta_{\rm H}$. According to the semiclassical theory for a single-band metal, the relation $\tan\theta_{\rm H} = \rho_{yx}/\rho_{xx} = \sigma_{xy}/\sigma_{xx} = \omega_c\tau_t$ should hold. However, if we calculate these values for the sample S3 in 14 T, $\tan\theta_H = \rho_{yx}/\rho_{xx} = 0.5$, whereas $\omega_c\tau_t = \mu_t B = 65$. Therefore, there is a two-orders-of-magnitude difference between what is purported to be the same parameter. This is significant, and it strongly supports the scenario that MR is actually governed by the Hall field rather than the scattering.

In the PL and Herring's model, the existence of inhomogeneity is essential. However, in our samples good crystallinity was confirmed by XRD and Laue analysis, and EPMA data confirmed that there is no segregation of constituent elements [28]. Also, the average donor distance $l_{\rm imp} \simeq n_{\rm SdH}^{-1/3} = 15$ nm and the Debye screening length $l_{\rm Debye} = 3$ nm [50] are both short; thus, the low temperature mean free path $\ell = v_F\tau_t = 600$ nm does not support the impurities to be the source of strong inhomogeneity. Whilst the linear relation between MR and μ_t [Fig. 3(e)] is along the lines with the prediction of PL model, the decline of the mobility in this case is due to phonon scattering and is not related to inhomogeneity. Therefore, while the essential spirit of the PL model is valid and the Hall field appears to be the fundamental source of the linear MR, the actual mechanism to bring about such a situation is obviously an open question.

Finally, we mention that in a recent wok on another 3D Dirac system, Cd_3As_2 [51], a gigantic MR was observed in very clean samples (with $\mu_t > 10^7$ cm^2/Vs) as a result of lifting of the strong protection from backscattering, which was reflected in the fact that μ_t was 10^4 times larger than μ_q; this is different from our situation. In more disordered samples of Cd_3As_2 with $\mu_t \simeq 10^4$ cm^2/Vs, a large linear MR was observed, but it starts from very low field and it persists to 300 K, both of which suggests that it is more in line with the PL model than the TlBiSSe case. Note that an important difference between Cd_3As_2 and TlBiSSe is the number of Dirac cones (two vs one), and the former has a peculiar anisotropy and an additional valley degrees of freedom.

In summary, we found that in the 3D Dirac semimetal TlBiSSe, a reduction in carrier density n leads to a rapid increase in the transport mobility μ_t and transverse magnetoresistance (MR). In samples with $n \simeq 10^{17}$ cm^{-3}, μ_t becomes 5×10^4 cm^2/Vs and linear MR whose magnitude reaches almost 10,000% in 14 T was observed at 1.8 K. This linear MR is governed by the perpendicular component of the magnetic field, and the large discrepancy between $\tan\theta_H$ and $\omega_c\tau_t$ points to the scenario that the Hall field is the fundamental source of the linear MR. Nevertheless, inhomogeneity does not seem to play an important role here, and the exact mechanism to produce the large liner MR is yet to be determined.

We thank R. Sato for help in crystal growths, and A. A. Taskin for helpful discussions. This work was supported by JSPS (KAKENHI 24540320 and 25220708), MEXT (Innovative Area "Topological Quantum Phenomena" KAKENHI), AFOSR (AOARD 124038), Inamori Foundation, and the Murata Science Foundation.

* Electronic address: mnovak@sanken.osaka-u.ac.jp
† Electronic address: y˙ando@sanken.osaka-u.ac.jp

[1] A. K. Geim and K. S. Novoselov, Nat. Mater. **6**, 183 (2007).
[2] M. Z. Hasan and C. L. Kane, Rev. Mod. Phys. **82**, 3045 (2010).
[3] X.-L. Qi and S.-C. Zhang, Rev. Mod. Phys. **83**, 1057 (2011).
[4] Y. Ando, J. Phys. Soc. Jpn. **82**, 102001 (2013).
[5] H. Fukuyama, Y. Fuseya, M. Ogata, A. Kobayashi, and Y. Suzumura, Physica B **407**, 1943 (2012).
[6] L. Li, J. G. Checkelsky, Y. S. Hor, C. Uher, A. F. Hebard, R. J. Cava, and N. P. Ong, Science **321**, 547 (2008).
[7] Z. Zhu, A. Collaudin, B. Fauque, W. Kang, and K. Behnia, Nat. Phys. **8**, 89 (2012).
[8] X. Wan, A. M. Turner, A. Vishwanath, and S. Y. Savrasov Phys. Rev. B **83**, 205101 (2011).
[9] O. Vafek and A. Vishwanath, Annual Rev. of Cond. Matter Phys. **5** 83 (2014).
[10] Z. Wang, Y. Sun, X.-Q. Chen, C. Franchini, G. Xu, H. Weng, X. Dai, and Z. Fang, Phys. Rev. B **85**, 195320 (2012).
[11] Z. K. Liu, B. Zhou, Y. Zhang, Z. J. Wang, H. M. Weng, D. Prabhakaran, S.-K. Mo, Z. X. Shen, Z. Fang, X. Dai, Z. Hussain, and Y. L. Chen, Science **343**, 864 (2014).
[12] S.-Y. Xu, C. Liu, S. K. Kushwaha, T.-R. Chang, J. W. Krizan, R. Sankar, C. M. Polley, J. Adell, T. Balasubramanian, K. Miyamoto, N. Alidoust, G. Bian, M. Neupane, I. Belopolski, H.-T. Jeng, C.-Y. Huang, W.-F. Tsai, H. Lin, F. C. Chou, T. Okuda, A. Bansil, R. J. Cava, and M. Z. Hasan, arXiv:1312.7624.
[13] Z. Wang, H. Weng, Q. Wu, X. Dai, and Z. Fang, Phys. Rev. B **88**, 125427 (2013).
[14] M. Neupane, S.-Y. Xu, R. Sankar, N. Alidoust, G. Bian, C. Liu, I. Belopolski, T.-R. Chang, H.-T. Jeng, H. Lin, A. Bansil, F. Chou, and M. Z. Hasan, Nat. Commun. **5**, 3786 (214).
[15] S. Borisenko, Q. Gibson, D. Evtushinsky, V. Zabolotnyy, B. Büchner, and R. J. Cava, Phys. Rev. Lett. **113**, 027603 (2014).
[16] T. Sato, K. Segawa, K. Kosaka, S. Souma, K. Nakayama, K. Eto, T. Minami, Y. Ando, and T. Takahashi, Nat. Phys. **7**, 840 (2011).
[17] S.-Y. Xu, Y. Xia, L. A. Wray, S. Jia, F. Meier, J. H. Dil, J. Osterwalder, B. Slomski, A. Bansil, H. Lin, R. J. Cava, and M. Z. Hasan, Science **332**, 560 (2011).
[18] A. A. Burkov and L. Balents, Phys. Rev. Lett. **107**, 127205 (2011).
[19] B. Singh, A. Sharma, H. Lin, M. Z. Hasan, R. Prasad, and A. Bansil, Phys. Rev. B **86**, 115208 (2012).
[20] I. Zeljkovic, Y. Okada, M. Serbyn, R. Sankar, D. Walkup, W. Zhou, M. Z. Hasan, F. Chou, L. Fu, and V. Madhavan, arXiv:1403.4906.
[21] J. C. Y. Teo, L. Fu, and C. L. Kane, Phys. Rev. B **78**, 045426 (2008).
[22] H.-J. Kim, K.-S. Kim, J.-F. Wang, M. Sasaki, N. Satoh, A. Ohnishi, M. Kitaura, M. Yang, and L. Li, Phys. Rev. Lett. **111**, 246603 (2013).
[23] D. Bulmash, C.-X. Liu, and X.-L. Qi, Phys. Rev. B **89**, 081106(R) (2014).
[24] T. Sato, K. Segawa, H. Guo, K. Sugawara, S. Souma, T. Takahashi, and Y. Ando, Phys. Rev. Lett. **105**, 136802 (2010).
[25] K. Kuroda, M. Ye, A. Kimura, S. V. Eremeev, E. E. Krasovskii, E. V. Chulkov, Y. Ueda, K. Miyamoto, T. Okuda, K. Shimada, H. Namatame, and M. Taniguchi, Phys. Rev. Lett. **105**, 146801 (2010).
[26] Y. L. Chen, Z. K. Liu, J. G. Analytis, J.-H. Chu, H. J. Zhang, B. H. Yan, S.-K. Mo, R. G. Moore, D. H. Lu, I. R. Fisher, S. C. Zhang, Z. Hussain, and Z.-X. Shen, Phys. Rev. Lett. **105**, 266401 (2010).
[27] K. Kuroda, G. Eguchi, K. Shirai, M. Shiraishi, M. Ye, K. Miyamoto, T. Okuda, S. Ueda, M. Arita, H. Namatame, M. Taniguchi, Y. Ueda, and A. Kimura, arXiv:1308.5521.
[28] See Supplemental Material at (URL to be inserted) for supplemental data and discussions.
[29] Y. Zhang, Y.-W. Tan, H. L. Stormer, and P. Kim, Nature **438**, 201 (2005).
[30] F. Yang, A. A. Taskin, S. Sasaki, K. Segawa, Y. Ohno, K. Matsumoto, and Y. Ando, Appl. Phys. Lett. **104**, 161614 (2014).
[31] R. Xu, A. Husmann, T. F. Rosenbaum, M.-L. Saboungi, J. E. Enderby, and P. B. Littlewood, Nature **390**, 57 (1997).
[32] A. A. Abrikosov: *Fundamentals of the Theory of Metals* (North-Holland, Amsterdam, 1988).
[33] J. Hu and T. F. Rosenbaum, Nat. Mater. **7**, 697 (2008).
[34] X. Wang, Y. Du, S. Dou, and C. Zhang, Phys. Rev. Lett. **108**, 266806 (2012).
[35] A. L. Friedman, J. L. Tedesco, P. M. Campbell, J. C. Culbertson, E. Aifer, F. K. Perkins, R. L. Myers-Ward, J. K. Hite, C. R. Eddy Jr., G. G. Jernigan, and D. K. Gaskill, Nano Lett., **10**, 3962 (2010).
[36] N. A. Porter and C. H. Marrows Sci. Rep. **2**, 565 (2012).
[37] N. V. Kozlova, N. Mori, O. Makarovsky, L. Eaves, Q. D. Zhuang, A. Krier, and A. Patane, Nat. Commun. **3** 1097 (2012).
[38] A. B. Pippard: *Magnetoresistance in Metals* (Cambridge University Press, Cambridge, U.K., 1989).
[39] The carrier density determined from the low-field R_H for the sample S3 is $n = 3.8 \times 10^{17}$ cm^{-3}.
[40] D. Shoenberg: *Magnetic Oscillations in Metals* (Cambridge University Press, Cambridge, U.K., 1984).
[41] S. Das Sarma and F. Stern, Phys. Rev. B **32**, 8442 (1985).
[42] I. A. Luk'yanchuk and Y. Kopelevich, Phys. Rev. Lett. **97**, 256801 (2006).
[43] H. Murakawa, M. S. Bahramy, M. Tokunaga, Y. Kohama, C. Bell, Y. Kaneko, N. Nagaosa, H. Y. Hwang, and Y. Tokura, Science **342**, 1490 (2013).
[44] A. A. Taskin, F. Yang, S. Sasaki, K. Segawa, and Y. Ando, Phys. Rev. B **89**, 121302(R) (2014).
[45] A. A. Abrikosov, Phys. Rev. B **58**, 2788 (1998).
[46] A. A. Abrikosov, Europhys. Lett. **49**, 789 (2000).
[47] C. Herring, J. Appl. Phys.**31**, 1939 (1960).
[48] M. M. Parish and P. B. Littlewood, Nature **426**, 162 (2003).
[49] J. Hu, M. M. Parish, and T. F. Rosenbaum, Phys. Rev. B **75**, 214203 (2007).
[50] We calculated the Debye screening length from $l_{\rm Debye} = [\epsilon k_B T/(ne^2)]^{1/2}$ with the dielectric constant $\epsilon \approx 20$ and $T = 1.8$ K.
[51] T. Liang, Q. Gibson, M. N. Ali, M. Liu, R. J. Cava, and N. P. Ong, arXiv:1404.7794.